New insights into the breathing phenomenon in ZIF-4

Jesus Gandara-Loe, Alexander Missyul, François Fauth, Luke L. Daemen, Yongqiang Q. Cheng, Anibal J. Ramirez-Cuesta, Peter I. Ravikovitch, Joaquin Silvestre-Albero*

Abstract: Structural changes in ZIFs upon adsorption remain a paradigm due to the sensitivity of the adsorption mechanism to the nature of the organic ligands and gas probe molecules. Synchrotron X-ray diffraction under *operando* conditions clearly demonstrates for the first time that ZIF-4 exhibits a structural reorientation from a narrow-pore (np) to a new expanded-pore (ep) structure upon N_2 adsorption, while it does not do so for CO_2 adsorption. The existence of an expanded-pore structure of ZIF-4 has also been predicted by molecular simulations. In simulations the expanded structure was stabilized by entropy at high temperatures and by strong adsorption of N_2 at low temperatures. These results are in perfect agreement with manometric adsorption measurements for N_2 at 77K that show the threshold pressure for the breathing at ~30 kPa. Inelastic neutron scattering (INS) measurements show that CO_2 is also able to promote structural changes but, in this specific case, only at cryogenic temperatures (5 K).

Table of Contents

Results and discussion

Results and Discussion

1. X-Ray Powder Diffraction (XRPD) data on the as-synthesized ZIF-4

The quality of the synthesized ZIF-4 crystals has been evaluated using synchrotron XRPD measurements. Figure S1 shows the pattern for the as-synthesized sample and the Rietveld refinement. The XRPD pattern of the desolvated sample exhibits a very good agreement with the theoretical one, thus confirming the quality of the synthesized crystals. At this point it is important to highlight the synthesis of ZIF-4 is quite challenging since small variations in the synthesis protocol gives rise to white powders with collapsed structures.

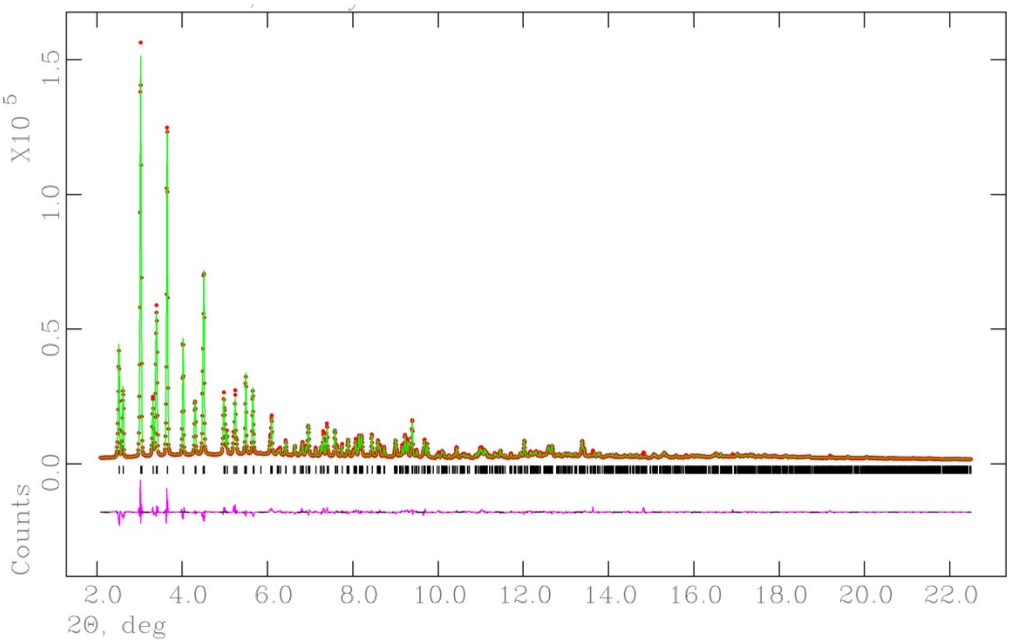

Figure S1. Rietveld refinement of the X-ray powder diffraction pattern of as-synthesized ZIF-4 performed using synchrotron XRPD. Initial model taken from Lewis et al. [1]

2. Textural and morphological characterization

The morphology of the synthesized crystals was evaluated using scanning electron microscopy (SEM). Figure S2 shows two representative images of the as-synthesized crystals. As it can be observed, the proposed synthesis approach gives rise to high quality crystals with rhombohedra morphology and with a crystal size in the micrometer-size range (average size *ca.* 625 μm±137μm).

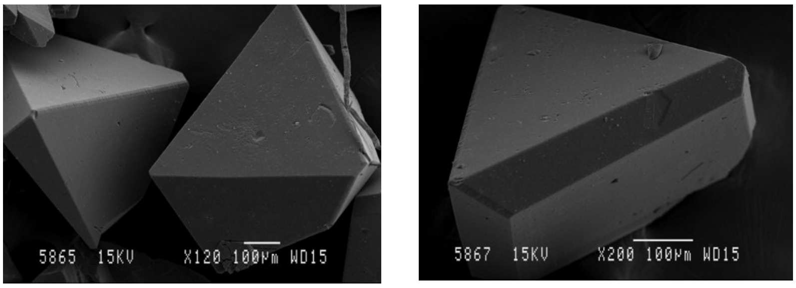

Figure S2. SEM images of the synthesize microcrystals of ZIF-4.

The textural properties of the synthesized samples were evaluated using nitrogen adsorption at 77 K. N_2 adsorption/desorption measurements were performed in a fully automated manometric equipment under very strict criteria to reach equilibrium. At this point it is important to highlight that the whole nitrogen isotherm for ZIF-4 crystals took approximately one week. As it can be observed in Figure 1 (main text), the amount of nitrogen adsorbed below $p/p_0 = 0.3$ is rather zero. Consequently, N_2 adsorption measurement in ZIF-4 does not allow calculating the monolayer capacity, and consequently, the BET surface area of ZIF-4.

3. Molecular simulations of ZIF-4 phase transition

Forcefield.

Molecular Dynamics simulations were performed with the forcefield based on the forcefield developed by Zhang et al [2]. These authors modified Amber forcefield to simulate N_2-induced transition in ZIF-8 [2]. The forcefield has been recently adopted by some of us to simulate the temperature-induced transition in ZIF-7 [3]. The major modification was to use the QEq charge equilibration scheme [4] to calculate partial atomic charges. The parameters are listed in Tables S1-S5. With this modification the forcefield predicts reliable structural properties of ZIF-8. In particular, it predicts anisotropic mechanical properties of ZIF-8 in reasonable agreement with experimental measurements [5] (see Table S6 below).

MD simulations

MD simulations were performed using Forcite code from Materials Studio 2018 from BIOVIA. First, we converted ZIF-4 structure to P1 and minimized it to obtain a dense structure at zero temperature. Starting with this structure we performed a series of short N*p*T simulations with progressively increasing temperature. This procedure mimics the experimental measurements of temperature induced phase transition in ZIF-7 [3] and ZIF-4 [6]. MD simulations we performed with 0.2 fs timestep, Nose-Hoover thermostat [7] with Q ratio 0.001, and anisotropic Parrinello-Raman [8] barostat as implemented by Martyna et al [9] with time constant of 0.1 ps. The length of simulations at each temperature was 1 ps. The temperature ramp was from 10 K to 1510 K with 450 steps. We used 3x2x2 supercell. Simulations were also performed with 2x2x2 and single unit cell to confirm the results. The use of a larger 3x2x2 supercell is preferred as it minimize fluctuations in volume and pressure.

Figure 4 (main text) shows typical simulation results. Starting from low temperature we observe first a transition from the ZIF-4 (LT) phase to ZIF-4 (HT) phase, in close agreement with the experimental measurements [6] for both unit cell parameters as well as the temperature of transition (150 K on the experiment, and ~200 K in simulations). Upon further heating we observe a transition to a pore-expanded ZIF-4 structure at ~1200K. The unit cell parameters of the predicted expanded structure are in very close agreement with the measurements for the N_2 loaded ZIF-4 at 77 K (Fig. 3, main text). Of course, this transition in simulations can't be observed experimentally upon heating because ZIF-4 would either decompose, undergo amorphization [10] or transition into a glassy state [11].

Grand Canonical Monte Carlo (GCMC) simulations.

GCMC simulations were performed to load the obtained expanded ZIF-4 structure with N_2 molecules at 77 K. To facilitate full loading, we performed simulations at 1000 kPa. We used TraPPE forcefiled for N_2 molecules [12] and n-pentane [13] and Lorentz-Berthelot combining rules for LJ interactions with ZIF-4 atoms.

After GCMC simulations we performed N*p*T simulations for expanded ZIF-4 loaded with N_2 molecules to confirm the stability of the structure and refine the unit cell parameters at 77 K.

Calculations of Vibrational Density of States.

Vibrational Density of States (VDOS) was calculated from MD simulations using Fourier transform of the velocity autocorrelation function *(VACF)* [14].

$$VACF(t)=\frac{v(0)\bullet v(t)}{v(0)\bullet v(0)}=\frac{1}{LN}\sum_{k}^{L}\sum_{i}^{N}v_i(t_k)\bullet v_i(t_k+t)$$

$$g(\omega) = \frac{1}{\sqrt{2\pi}} \int_{-\infty}^{\infty} VACF(t) e^{-i\omega t} dt$$

To capture low frequency modes responsible for the phase transitions between different polymorphs of ZIF-4, the production simulations were performed for 50 ps. VDOS for each individual atom were weighted according to the atomic masses.

$$g(\omega) = \sum_{j=1}^{N} m_j g_j(\omega)$$

For a given structure simulations were performed in the NVT ensemble at 300 K with a unit cell taken as an average from NPT simulations. We checked that the thermostat and barostat did not affect the calculated VDOS frequences. Essentially identical results were obtained from NPT simulations, NVT simulations, and from NVE simulations (performed after NVT so that the temperature was close to the desired temperature).

Figure S3 shows comparison between experimental INS spectra, DFT calculated spectra and VDOS from classical MD simulations using forcefield.

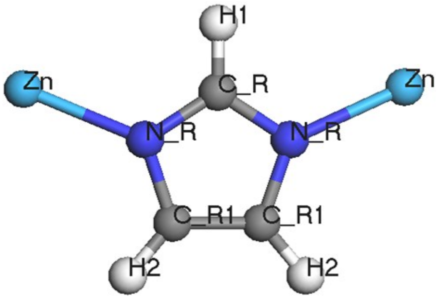

Table S1. Lennard-Jones parameters and partial charges for ZIF-4 simulations

	U, kcal/mol	R_0= 2^(1/6) σ, A	q, e [a]
C_R	0.0567	3.8512	0.207
C_R1	0.0567	3.8512	0.010
H1	0.0238	2.8859	0.119
H2	0.0238	2.8859	0.098
N_R	0.0373	3.6604	-0.303
Zn	0.067	2.7635	0.128

[a] Average charges. Charges were calculated using the QEq procedure [4] for the reported ZIF-4(HT) structure [6] and were kept constant during subsequent calculations.

Table S2. Bond stretch parameters for ZIF-4 simulations

$$U_{stretch} = \frac{K_0}{2}(R - R_0)^2$$

	R_0, A	K_0, kcal/mol/A^2
C_R1 – C_R1	1.346	1036
C_R - H1	0.929	734
C_R1 – H2	0.929	734
N_R – C_R	1.339	976
N_R – C_R1	1.371	820
Zn – N_R	1.987	172

Table S3. Angle bend parameters for ZIF-4 simulations

$$U_{bend} = \frac{K_0}{2}(\theta - \theta_0)^2$$

	θ_0	K_0, kcal/mol/rad^2
C_R – N_R – C_R1	105.24	140
C_R1 – C_R1 – H2	125.67	100
N_R – C_R – H1	123.89	100
N_R – C_R – N_R	112.17	140
N_R – C_R1 – C_R1	108.67	140
N_R – C_R1 – H2	125.66	100
N_R – Zn – N_R	109.47	21
Zn – N_R – C_R	127.5	100
Zn – C_R – C_R1	128	70

Table S4. Dihedral torsion parameters for ZIF-4 simulations.

$$U_{torsion} = \frac{1}{2}\sum_j B_j\left(1 - d_j\, cos[n_j\, \phi]\right)$$

	B, kcal/mol	d	n
Zn - N_R - C_R - H1	0.2	1	2
Zn - N_R - C_R - N_R	0.2	1	2
Zn - N_R - C_R1 - C_R1	0.2	1	2
Zn - N_R - C_R1 - H2	0.2	1	2
N_R - Zn - N_R - C_R	0.348	-1	3
N_R - Zn - N_R - C_R1	0.348	-1	3
H2 - C_R1 - C_R1 - H2	8	1	2
N_R - C_R1 - C_R1 - H2	8	1	2
N_R - C_R1 - C_R1 - N_R	8	1	2
C_R1 - N_R - C_R - H1	8.3	1	2
C_R1 - N_R - C_R - N_R	9.6	1	2
C_R1 - C_R1 - N_R - C_R	9.6	1	2
C_R - N_R - C_R1 - H2	9.6	1	2

Table S5. Improper torsion parameters for ZIF-4 simulations

$$U_{improper} = \frac{K_0}{2}\left(1 - cos[n\,\chi - \chi_0]\right)$$

	K_0, kcal/mol	n	χ_0
C_R – N_R – N_R – H1	2.2	2	0
C_R1 – C_R1 – H2 – N_R	2.2	2	0
Zn - N_R - C_R1 - C_R	2.0	2	0

Table S6. Reference calculations of anisotropic mechanical properties of ZIF-8 in comparison with experimental data.

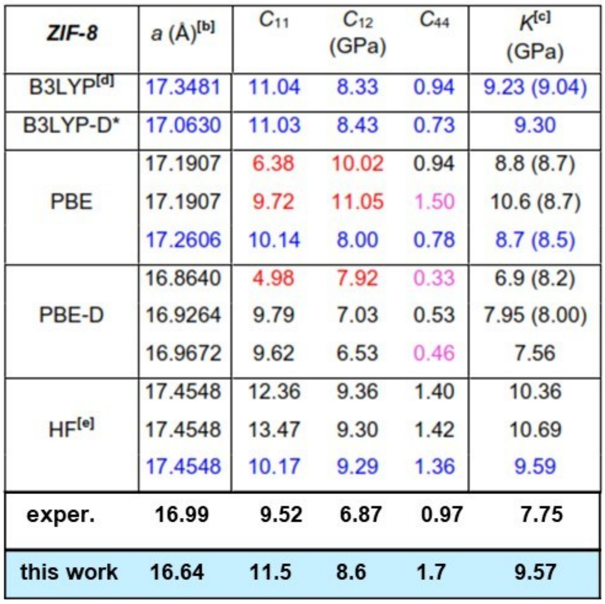

ZIF-8	*a* (Å)[b]	C_{11}	C_{12} (GPa)	C_{44}	*K*[c] (GPa)
B3LYP[d]	17.3481	11.04	8.33	0.94	9.23 (9.04)
B3LYP-D*	17.0630	11.03	8.43	0.73	9.30
PBE	17.1907	6.38	10.02	0.94	8.8 (8.7)
	17.1907	9.72	11.05	1.50	10.6 (8.7)
	17.2606	10.14	8.00	0.78	8.7 (8.5)
PBE-D	16.8640	4.98	7.92	0.33	6.9 (8.2)
	16.9264	9.79	7.03	0.53	7.95 (8.00)
	16.9672	9.62	6.53	0.46	7.56
HF[e]	17.4548	12.36	9.36	1.40	10.36
	17.4548	13.47	9.30	1.42	10.69
	17.4548	10.17	9.29	1.36	9.59
exper.	**16.99**	**9.52**	**6.87**	**0.97**	**7.75**
this work	**16.64**	**11.5**	**8.6**	**1.7**	**9.57**

Experimental unit cell parameters (*a*), anisotropic elastic constants (C_{11}, C_{12}, C_{44}) and bulk modulus (*K*), *ab initio* HF and DFT calculations (PBE and B3LYP functionals) are from Ref. [5]. Forcefield calculations from this work – last row.

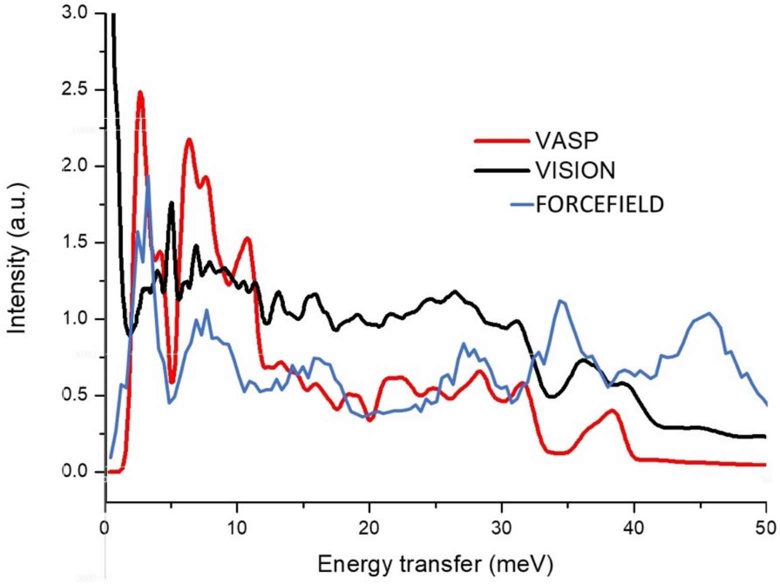

Figure S3. Vibrational Density of States calculated from forcefield model of high-density ZIF-4 structure at 50 K in comparison with INS and DFT (VASP)_calculations. Forcefield calculations were performed with the ZIF-4 (LT) structure (V=3160 A^3).

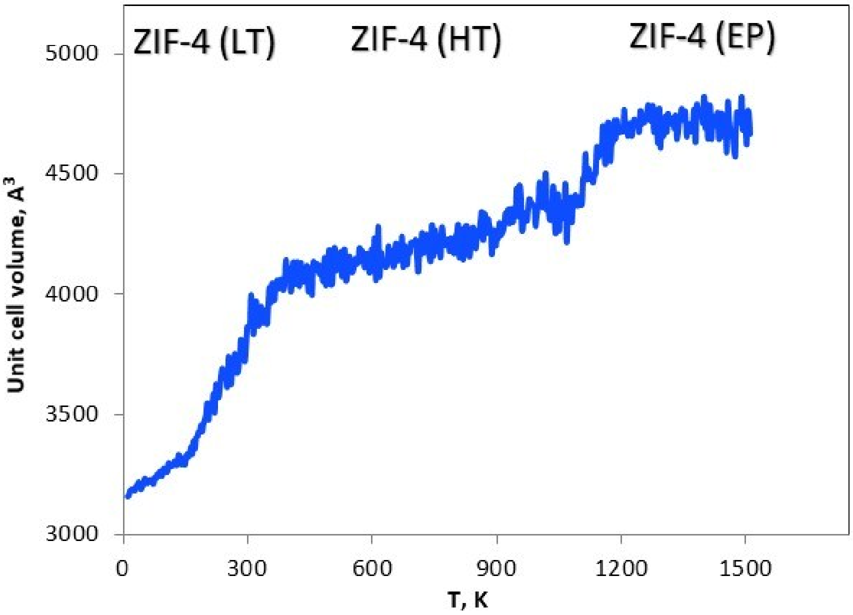

Figure S4. Unit cell volume evolution during Molecular Dynamics simulation of the phase transitions in ZIF-4 upon heating. The narrow pore structure ZIF-4 (LT) transitions first into the open pore structure ZIF-4 (HT) at around 200-300 K, and then into expanded pore ZIF-4 (ep) structure.

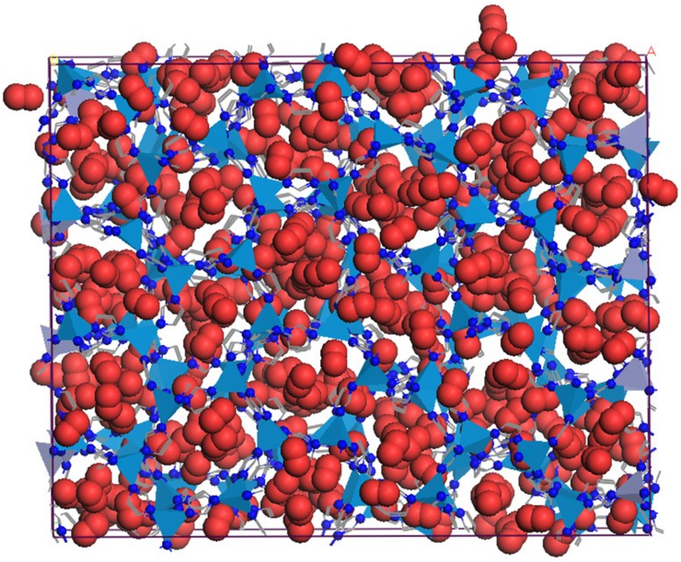

Figure S5. Snapshot from the MD simulations of the pore-expanded ZIF-4 (ep) structure with N_2 molecules at the loading of 10.3 mmol/g at 77 K. The structure is viewed from the Y direction.

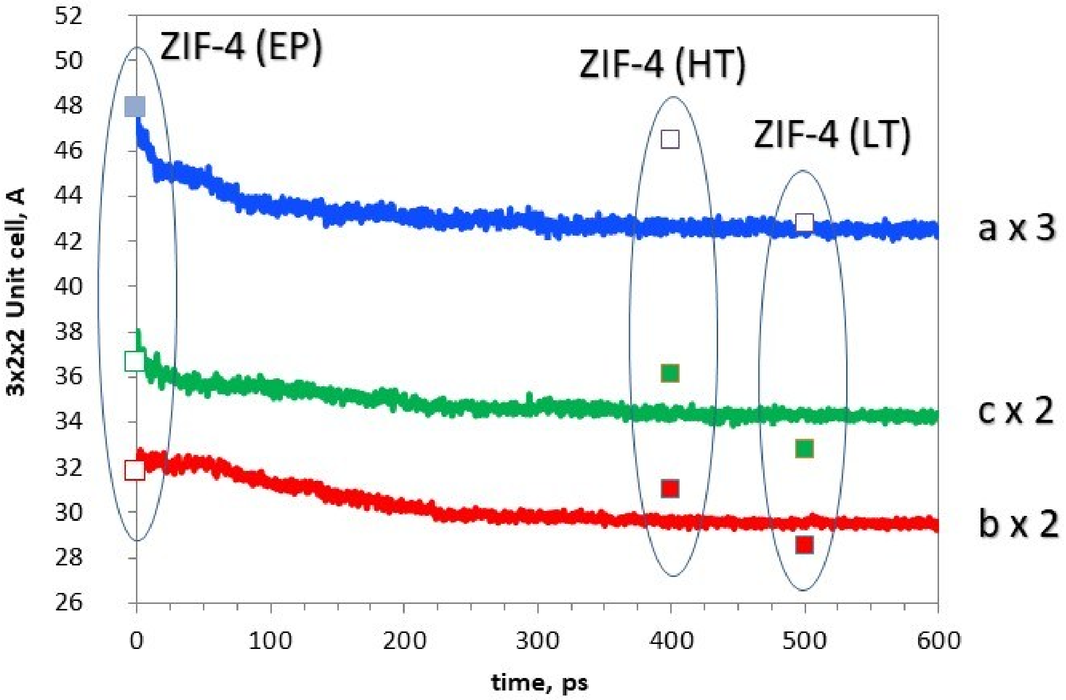

Figure S6. MD N*p*T simulations at 77 K of an empty ZIF-4 starting from the pore-expanded ZIF-4 (ep) structure. Parameters for the reported experimental ZIF-4 structures are shown as symbols. ZIF-4 (ep) is from this work, ZIF-4 (HT) and ZIF-4 (LT) are from Ref. 6.

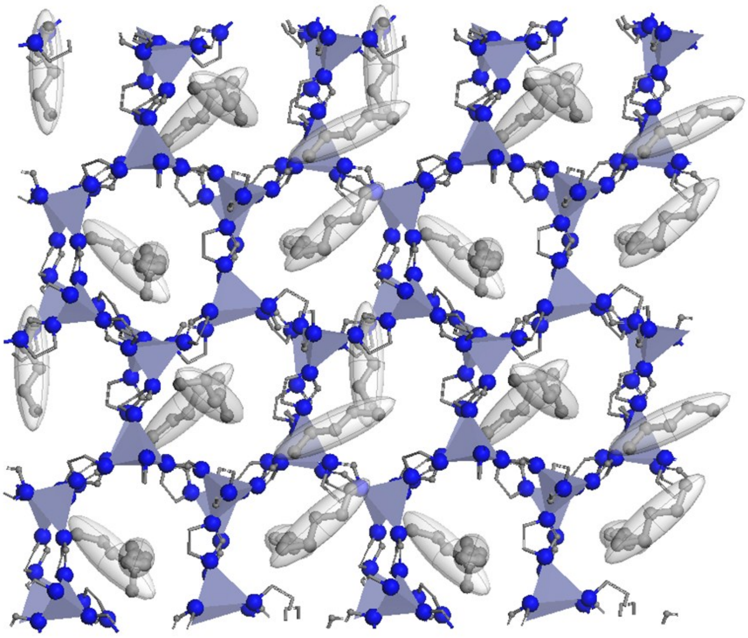

Figure S7. Snapshot from the GCMC simulations of the pore-expanded ZIF-4 (ep) structure with pentane molecules at the loading of 2.5 mmol/g. The structure is viewed from the Y direction.

4. Gas adsorption and Synchrotron X-Ray Powder Diffraction data for CO_2

N_2 measurements described above were complemented by CO_2 adsorption/desorption tests at 273 K. Figure S8 shows the CO_2 adsorption isotherm up to atmospheric pressure. The total adsorption capacity of ZIF-4 is 3.2 $mmol\cdot g^{-1}$ at 273 K. Assuming a CO_2 liquid density of 1.023 $g\cdot cm^{-3}$ at 273 K, the total pore volume accessed by CO_2 (estimated from the Dubinin-Raduschkevich equation) is around 0.21 $cm^3\cdot g^{-1}$. Taking into account the microporous nature of ZIF-4 (pore cavities are around 0.49 nm), the amount of N_2 and CO_2 adsorbed as a liquid must be the same assuming the validity of the Gurvich rule in these kind of materials. However, the large difference between the pore volume obtained by N_2 (0.43 $cm^3\cdot g^{-1}$) and the one obtained from the CO_2 adsorption data (0.21 $cm^3\cdot g^{-1}$), together with the concave shape and fast kinetics of the CO_2 adsorption isotherms clearly ruled out the presence of a phase transition upon CO_2 adsorption from a narrow-pore (np) to an expanded-pore (ep) structure.

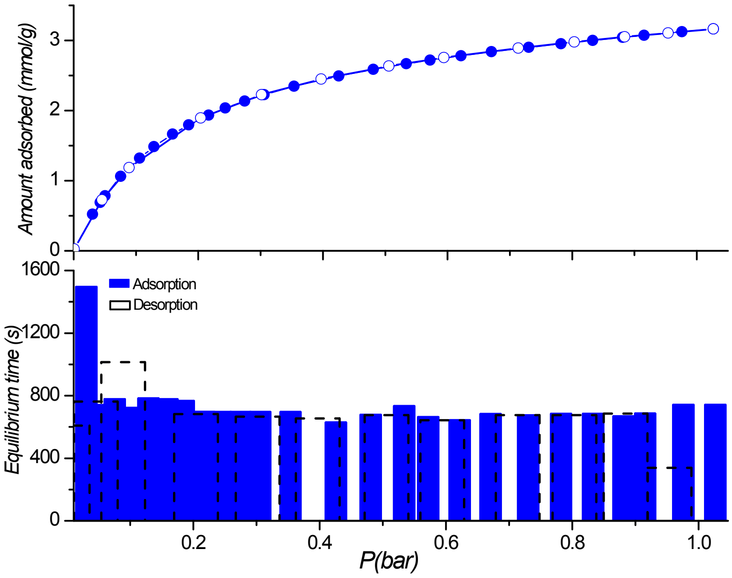

Figure S8. (Upper panel) CO_2 adsorption (full symbols)/desorption (empty symbols) isotherms at 273 K for ZIF-4. (Lower panel) Time requested to reach equilibrium for each of the adsorption and desorption points at the isotherm.

Figure S9 shows the XRD pattern for the ZIF-4 sample at 298 K before and after dosing CO_2 up to 103 kPa. As it can be appreciated, the XRD pattern of ZIF-4 crystals does not exhibit any change upon CO_2 incorporation, neither after a subsequent evacuation treatment. These results are in close agreement with the CO_2 adsorption isotherms described above and confirm the assumption that CO_2 at room temperature and 103 kPa is not able to promote in ZIF-4 the phase transition from the narrow-pore to the expanded-pore structure.

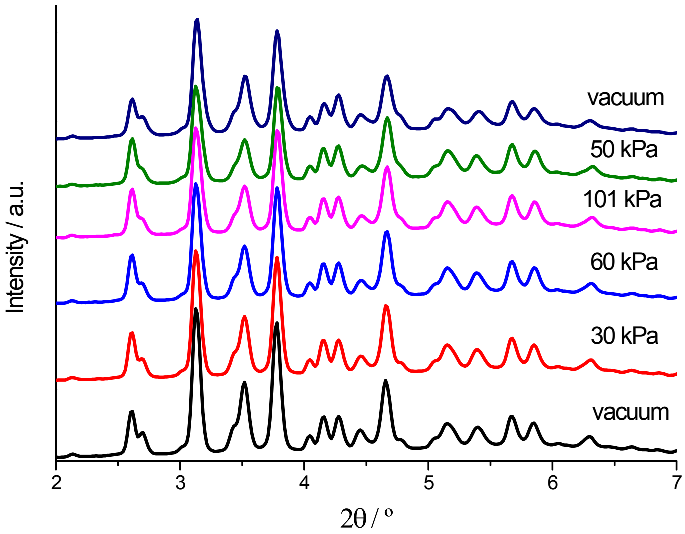

Figure S9. Synchrotron XRPD pattern for ZIF-4 at 298 K before and after introduction of CO_2 up to 103 kPa.

5. Inelastic neutron scattering analysis

INS measurements were performed at the high-resolution VISION spectrometer at the Spallation Neutron Source at Oak Ridge National laboratory (USA). The INS spectra cover an energy transfer range up to 250 meV, and shows the most relevant rotational and vibrational modes of the zeolitic-imidazole framework. The INS of ZIF-4 can be divided in two regions: i) the low energy transfer region (0-50 meV), which reveals the dynamics of the framework opening and contains torsion, vibrational and librational modes of the imidazole linker, ii) the middle-high energy region (50-250 meV), which contains ring deformation modes and bending modes for the C-C and C-H bonds. Modeling of bare ZIF-4 was performed using the Vienna Ab initio Simulation Package (VASP) [15]. The calculation used Projector Augmented Wave (PAW) method [16,17] to describe the effects of core electrons, and Perdew-Burke-Ernzerhof (PBE) [18] implementation of the Generalized Gradient Approximation (GGA) for the exchange-correlation functional. Energy cutoff was 800eV for the plane-wave basis of the valence electrons. The electronic structure was calculated on a 2×2×2 Monkhorst-Pack mesh. The total energy tolerance for electronic energy minimization was 10^{-8} eV, and for structure optimization it was 10^{-7} eV. The maximum interatomic force after relaxation was below 0.001 eV/Å. The optB86b-vdW functional [19] for dispersion corrections was applied. The vibrational eigen-frequencies and modes were then calculated by solving the force constants and dynamical matrix using Phonopy [20].The OClimax software [21] was used to convert the DFT-calculated phonon results to the simulated INS spectra.

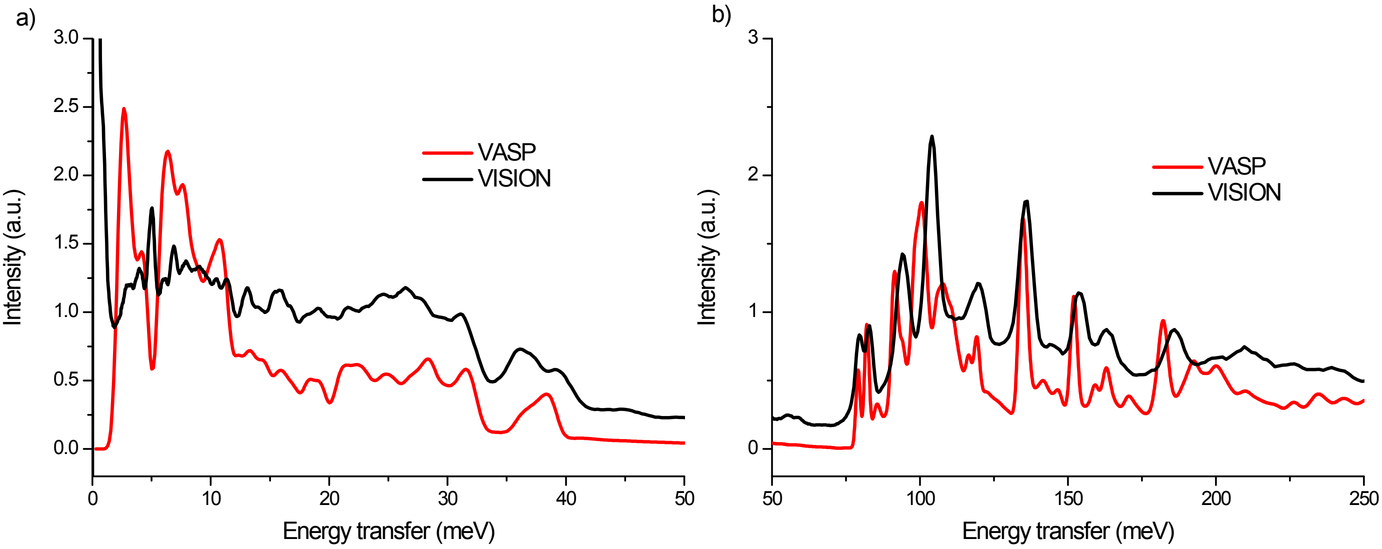

Figure S10. Inelastic neutron scattering spectra of ZIF-4 at 5 K in the low (left) and high (right) energy transfer range. The simulated spectra using VASP model is also included (red).

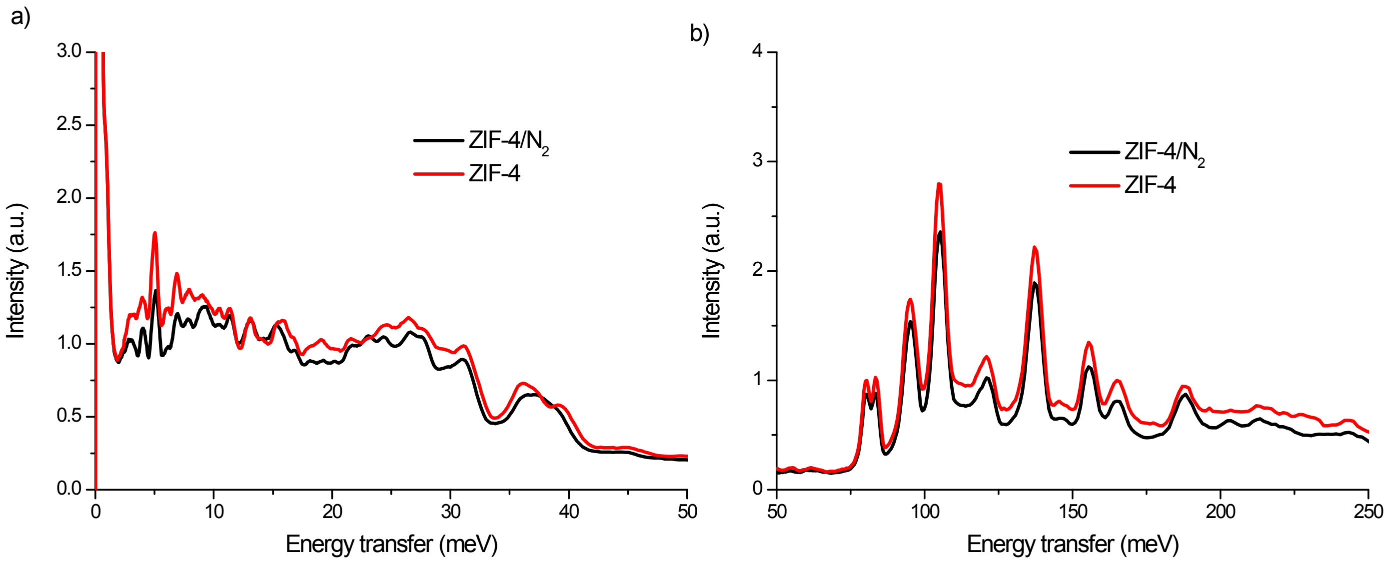

Figure S11. Inelastic neutron scattering spectra of ZIF-4 at 5 K before and after the incorporation of 103 kPa of N_2 at 77 K. After incorporation of N_2 the sample was cooled down to 5 K before the INS measurement. Low (left) and high (right) energy transfer range are shown.

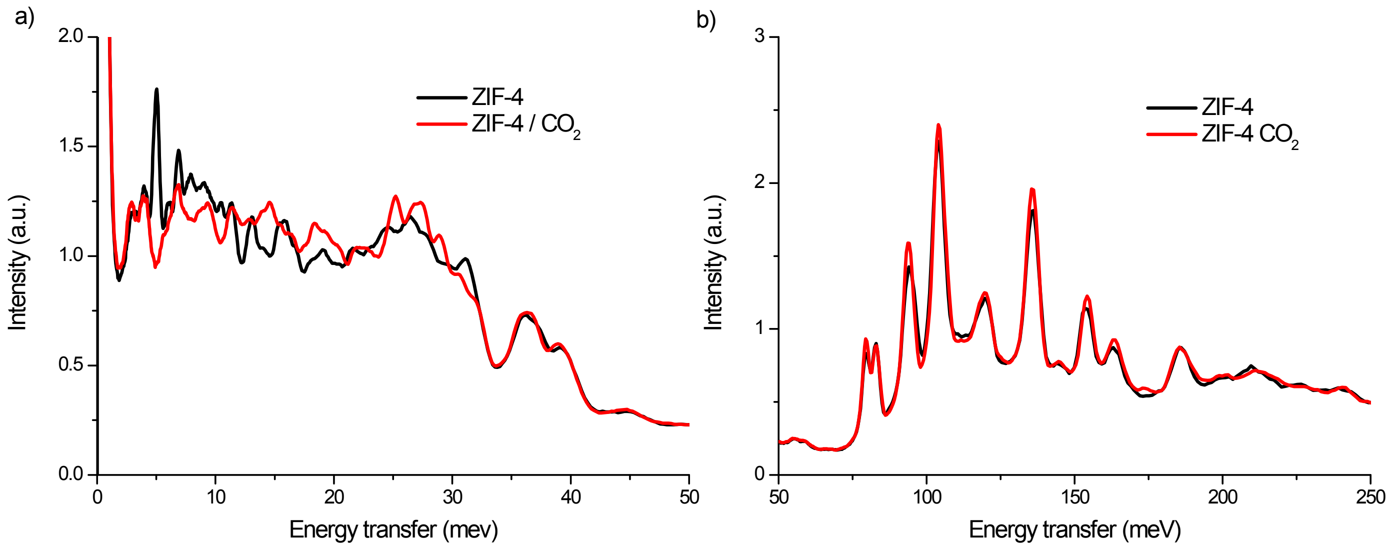

Figure S12. Inelastic neutron scattering spectra of ZIF-4 at 5 K before and after the incorporation of 103 kPa of CO_2 at 298 K. After incorporation of CO_2 the sample was cooled down to 5 K before the INS measurement. Low (left) and high (right) energy transfer range are shown.

References

[1] D.W. Lewis, A. Rabdel Ruiz-Salvador, A. Gómez, L. Marleny Rodríguez-Albelo, F.-X. Coudert, B. Slater, A.K. Cheetham, C. Mellot-Draznieks, *CrystEngComm* **2009**, *11*, 2272-2276.

[2] L. Zhang, Z. Hu, J. Jiang, *J. Am. Chem. Soc.* **2013**, *135*, 3722.

[3] Y. Du, B. Wooler, M. Nines, P. Kortunov, S.C. Paur, J. Zengel, S.C. Weston, P.I. Ravikovitch, *J. Am. Chem. Soc.*, **2015**, *137*, 13603-13611.

[4] A.K. Rappe, W.A. Goddard, *J. Phys. Chem.* **1991**, *95*, 3358.

[5] J.-C. Tan, B. Civalleri, B.; C.-C. Lin, L. Valenzano, R. Galvelis, P.-F. Chen, T.D. Bennett, C. MellotDraznieks, C.M. Zicovich-Wilson, A.K. Cheetham, *Phys. Rev. Lett.* **2012**, *108*, 095502.

[6] M.T. Wharmby, S. Henke, T.D. Bennett, S.R. Bajpe, I. Schwedler, S.P. Thompson, F. Gozzo, P. Simoncic, C. Mellot-Draznieks, H. Tao, Y. Yue, A.K. Cheetham, Angew. Chem. Int. Ed., 2015, 54, 6447-6451.
[7] S. Nosé, *Prog. Theor. Phys., Suppl.*, 1991, *103*, 1-46.
[8] M. Parrinello, M., A. Rahman, *J. Appl. Phys.*, **1981**, *52*, 7182-7190.
[9] G.J. Martyna, J. T. Tobias, and M. L. Klein, *J. Chem. Phys.* **1994**, *101*, 4177-4189.
[10] T.D. Bennett, D. A. Keen, J.-C. Tan, E. R. Barney, A. L. Goodwin, A.K. Cheetham*, Angewandte Chemie Int Ed*, **2011**, *50,* 3067-3071.
[11] T.D. Bennett et al, *J. Am. Chem. Soc*. **2016**, *138*, 3484−3492.
[12] J.J. Potoff, J.I. Siepmann, *AIChE J.*, **2001**, *47*, 1676.
[13] C D. Wick, J.I. Siepmann, W.L. Klotz, M.R. Schure, M.R. *J. Chromatography A,* **2002**, *954*, 181.
[14] S.-T. Lin, M. Blanco, W.A. Goddard III, *J. Chem. Phys.*, **2003**, *119*, 11792-11805.
[15] G. Kresse, J. Furthmüller, *Phys. Rev. B,* **1996**, *54*, 11169-11186.
[16] P.E. Blochl, *Phys. Rev. B*, **1994**, *50*, 17953-17979.
[17] G. Kresse, D. Joubert, *Phys. Rev. B*, **1999**, *59*, 1758-1775.
[18] J.P. Perdew, K. Burke, M. Ernzerhof,. *Phys. Rev. Lett.*, **1996**, *77*, 3865-3868.
[19] J. Klimeš, D.R. Bowler, A. Michaelides, *J. Phys.: Cond. Matt.* **2010**, *22*, 022201.
[20] T. Togo, I. Tanaka, *Scr. Mater*, **2015**, *108*, 1-5.
[21] Y.Q. Cheng, L.L. Daemen, A.I. Kolesnikov, A.J. Ramirez-Cuesta, *J. Chem. Theory and Computation*, **2019**, *15*, 1974-1982.